**Seventh International Conference on Computational Fluid Dynamics (ICCFD7), Big Island, Hawaii, July 9-13, 2012**

**ICCFD7-2701**

# Delayed-Detached Eddy Simulation for Optical Path Control on Backward-Facing Step Flow

C. Y. Lee*, S. H. Park*, S. Cho**and I. Lee**
Corresponding author: pish@konkuk.ac.kr

* Department of Aerospace Information Engineering, Konkuk University, Seoul, South Korea.
** Department of Aerospace Engineering, KAIST, Daejeon, South Korea.

**Abstract:** A feedback flow control is designed to reduce the aero-optical distortions behind a backward facing step. The delayed-detached eddy simulation, based on the Spalart-Allmaras turbulence model, is developed to simulate the unsteady density variations caused by the shear layer. A database from simulations of both an unforced baseline flow and open-loop forced flows is built using the proper orthogonal decomposition. An Artificial Neural Network and an Auto-Regressive eXogenous model are used to build a reduced order model of the flow field. Closed loop controllers for a suction-blowing actuator were simulated using the reduced order model. Finally, the actuation results from the closed-loop simulation are validated by re-computing the forced flow. The results show that aero-optical distortions can be reduced via the feedback flow controller based on the reduced order model.

*Keywords:* Delayed-Detached Eddy Simulation, Backward Facing Step, Feedback Flow Control, Reduced Order Model, Optical Path Difference

## 1 Introduction

Aero-optical aberrations have been a major issue for optical system design since such systems became airborne. Target-seeking missiles, airborne surveillance systems, and airborne laser weapon systems are examples of such systems that may be affected by aero-optical aberrations. The transmission of a collimated light beam through a medium with time and spatial variation of density results in a distorted wave front. The cause of such aberrations can be classified into two categories: the long-distance atmospheric problem and turbulent unsteady flows in the near-field [1]. The former problem is concerned with the path length, which is much longer than the viewing aperture; aberrations caused by this problem can be compensated for to a reasonable extent by modern adaptive optics [2]. These modern adaptive optical correction methods, however, are incapable of resolving the latter problem of turbulent flow immediately surrounding the optical system [3].

In the near-field aero-optics problem, the turbulent flows of interest are compressible boundary layers and free-shear layers. There has been much work done in investigating the effects of high-speed, turbulent boundary layers on optical aberrations. Cress et al. [4,5] have investigated the relationship between aero-optical measurements and flow characteristics such as Mach number, boundary layer displacement thickness, and wall heating. Scaling relationships for the root-mean-square (RMS) of the optical path difference (OPD) were suggested and shown to be consistent with

experimental data. There have been several experiments investigating the aspects of free shear layers in two-dimensional and three-dimensional turrets [6,7]. The free shear layer generated behind a turret forms large periodic structures that are due to the layer's natural instability. These structures are the source of density variations that cause optical aberrations. Smith et al. [8] investigated the aero-optical change in the boundary layer due to a small--on the order of 10-20 % of the boundary layer thickness--backward facing step and suggested a simple model to account for step effects on the boundary layers downstream of the backward facing step.

In an attempt to reduce these optical aberrations, Wittich et al. [9] performed an investigation with a beam passing through a shear layer with a variety of vortex generating devices. These passive flow control devices showed significant effects on the optical aberrations. The performance of passive flow control devices, however, was limited to the designed flow state; to overcome this limitation, a feedback flow control system was recommended. A feedback flow control system provides an extension to the passive flow control by sensing the instantaneous flow state and altering its output to account for its current flow state. Seidel et al. [10,11] showed promising results for feedback flow control strategies that reduced optical aberrations behind a large backward facing step. Their feedback flow control strategy is, first, to build a flow state database for unforced and open-loop forced flows. The delayed detached eddy simulations (DDES), based on the Spalart-Allmaras turbulence model, were employed in two-dimensional space to reduce the computational cost. Second, the obtained database was analyzed using the proper orthogonal decomposition (POD) and was then used to formulate a reduced order model (ROM) based on a wavelet neural net (WNN). Their results with the WNN model showed that a 35% reduction of optical aberrations is possible.

Spalart et al. [12] suggested the detached eddy simulation (DES) method based on the one-equation Spalart-Allmaras (S-A) turbulence model [13] for RANS applications. The S-A DDES is a hybrid Reynolds Averaged Navier Stokes (RANS) Large Eddy Simulation (LES) approach. The basic idea of the DES method is to use the S-A RANS turbulence model in the near wall region and to use SGS modeling in the separated region, in order to yield results that are comparable to those of the LES approach. The first formulation of Spalart's DES, denoted as DES97 [12], relies on grid size to act as an LES model; this reliance presented problems for ambiguous-sized grids by acting as an LES on unwanted regions and causing laminarization of the turbulent boundary layer. The delayed DES (DDES) method was introduced to mitigate this reliance on grid sizes by adopting a blending function from the $k-\omega$ Shear Stress Transport (SST) turbulence model [14]. The inherently three-dimensional and time-dependent DDES technique is known to be greatly dependent on the grid densities [14]; there have been many suggestions on how the DES length scale can be modeled [15-17].

In this paper, a feedback flow controller is designed in order to reduce the aero-optical distortions behind a backward facing step. A three-dimensional preconditioned compressible CFD solver using the S-A DDES technique is developed to simulate the unsteady turbulent flow over the backward facing step of Driver and Seegmiller [18]. The experimental result of Driver and Seegmiller is used for the validation of the numerical results. The three-dimensional unforced baseline flow and the open-loop forced flow database are reduced to two-dimensional data by a spatial averaging in the periodic direction. From the reduced two-dimensional data, the root-mean-square of the OPD is obtained at each streamwise location and these results are analyzed using POD. The resulting POD spatial modes and modal amplitudes are then used to formulate a ROM based on the artificial neural network and the auto-regressive exogenous (ANN-ARX) model [19]. The ANN-ARX model is investigated for closed-loop control to reduce aero-optical distortions.

# 2 Numerical Approach

## 2.1 Governing Equations

The preconditioned form of the compressible Navier-Stokes equations [20,21] can be written as

$$\mathbf{\Gamma}\frac{\partial \mathbf{Q}}{\partial t}+\frac{\partial\left(\mathbf{F}_i-\mathbf{F}_{vi}\right)}{\partial x_i}=0 \tag{1}$$

where $\mathbf{Q}$ is the primitive flow variable vector, and $\mathbf{F}_i$ and $\mathbf{F}_{vi}$ are the inviscid and viscous fluxes in

each direction, respectively :

$$\mathbf{Q}=\begin{bmatrix} p \\ u_i \\ T \end{bmatrix},\ \mathbf{F}_i=\begin{bmatrix} \rho u_i \\ \rho u_i u_j + p\delta_{ij} \\ \rho u_i H \end{bmatrix},\ \mathbf{F}_{vi}=\begin{bmatrix} 0 \\ \tau_{ij}+\tau_{ij}^* \\ u_i\left(\tau_{ij}+\tau_{ij}^*\right)-q_j \end{bmatrix} \tag{2}$$

Here, $\rho$, $p$, and $T$ are the density, pressure, and temperature; $u_i$ and $u_j$ are the Cartesian velocity components. $H=e+p/\rho=C_pT$ is the total enthalpy, where $e$ is the total energy. $q_i$ is the heat fluxes in each direction and the quantities $\tau_{ij}$ and $\tau_{ij}^*$ are the laminar and turbulent stresses, respectively.

The molecular viscosity is determined by the Sutherland law while the eddy viscosity, $\mu_t$, to determine the turbulent stresses, is defined by:

$$\mu_t=\rho\tilde{\nu}f_{v1} \tag{3}$$

The kinematic viscosity, $\tilde{\nu}$, is obtained from the S-A RANS turbulence model.

$$\frac{\partial\tilde{\nu}}{\partial t}+u_j\frac{\partial\tilde{\nu}}{\partial x_j}=C_{b1}\left[1-f_{t2}\right]\tilde{S}\tilde{\nu}+\left(\frac{C_{b1}}{k^2}f_{t2}-C_{w1}f_w\right)\left(\frac{\tilde{\nu}}{d}\right)^2+\frac{C_{b2}}{\sigma}\left(\frac{\partial\tilde{\nu}}{\partial x_j}\right)^2+\frac{1}{\sigma}\frac{\partial}{\partial x_j}\left[\left(\nu+\tilde{\nu}\right)\frac{\partial\tilde{\nu}}{\partial x_j}\right] \tag{4}$$

where the first term is the production term, the second term is the dissipation term, and the last two terms are the diffusion terms:

$$f_{t2}=1.2e^{\left(-0.5\chi^2\right)},\quad \chi=\frac{\tilde{\nu}}{\nu},\quad \tilde{S}=\Omega+\frac{\tilde{\nu}f_{v2}}{k^2d^2},\quad f_{v2}=1-\frac{\chi}{1+\chi f_{v1}},\quad C_{w1}=\frac{C_{b1}}{k^2}+\frac{\left(1+C_{b2}\right)}{\sigma}$$

$$f_{v1}=\frac{\chi^3}{\chi^3+C_{v1}^3}\quad f_w=\left[\frac{g^{-6}+C_{w3}^{-6}}{1+C_{w3}^{-6}}\right]^{-\frac{1}{6}}\quad g=r+C_{w2}\left(r^6-r\right)\quad r=\frac{\tilde{\nu}}{\tilde{S}k^2d^2}$$

and the coefficients are given as,

$$C_{b1}=0.1355,\quad C_{b2}=0.622,\quad k=0.41,\quad \sigma=2/3,$$
$$C_{w3}=2.0,\quad C_{v1}=7.1,\quad C_{w3}=0.3$$

The DDES method replaces the wall distance, $d$, appearing in the production and the dissipation terms, directly and indirectly, with a new length scale, $\tilde{l}$, given as:

$$\tilde{l}=d-f_d\max\left(0,d-C_{DES}\Delta\right) \tag{5}$$

where $C_{DES}=0.65$, and the blending function, $f_d$, is given as:

$$f_d=1-\tanh\left(\left[8r_d\right]^3\right) \tag{6}$$

and

$$r_d=\frac{\nu+\tilde{\nu}}{\sqrt{U_{ij}U_{ij}}k^2d^2} \tag{7}$$

Similar to that of $r$ given in S-A RANS, if $r_d$ becomes 1, it acts as a RANS; as it approaches 0 it acts as a DDES. The filter width $\Delta$ is the subgrid length scale, which depends on the grid size, and which was first suggested in the DES97 model as:

$$\Delta=\max\left(\Delta x,\Delta y,\Delta z\right) \tag{8}$$

where it takes the longest dimension of the grid cell as its filter length. However, it has been found that using the cubic root of the grid cell volume, as:

$$\Delta=\sqrt[3]{\left(\Delta x\,\Delta y\,\Delta z\right)} \tag{9}$$

is less dissipative and closer to the LES formulation in the separated flow [16]. Both length scales are tested along with various grid sizes for the present problem.

## 2.2 Numerical Schemes

The numerical flux function at the cell interface is simply written as:

$$F_{i+\frac{1}{2}} = \frac{1}{2}\left(F_R + F_L\right) - \frac{\sigma}{2}\Gamma|\Lambda|\Delta Q \tag{10}$$

where $\Delta Q = Q_R - Q_L$ . $F_R$ and $F_L$ are fluxes at each side of the cell interface. $|\Lambda|$ is defined by $|\Lambda| = diag\left(\sigma[\Gamma\mathrm{A}], u\delta_{jj}, u\right)$ [23], which replaces the flux Jacobian matrix of the inviscid flux. This numerical flux function is thought of as a scalar dissipation, whereas the baseline preconditioned Roe scheme has a matrix dissipation. The spectral radius of the preconditioned Jacobian matrix is only applied to the continuity equation's dissipation term, whereas the momentum and energy equations are not affected. It has been found that this modified flux formulation preserves the stability and accuracy of unsteady computations. For the high-order reconstruction of flow variables, a 5$^{th}$-order accurate upwind scheme without flux limiter is employed for the inviscid fluxes and a 4$^{th}$-order accurate central difference scheme is applied to the discretization of the viscous fluxes.

The 2$^{nd}$-order backward differencing method is used to advance the solution in the physical time. The preconditioned dual-time stepping method [24] with a diagonalized alternating direction implicit (DADI) scheme [21] is applied to the preconditioned system at each physical time step. The present unsteady preconditioning scales the artificial dissipation in the flux function as well as improving the pseudo-time convergence efficiency regardless of the physical time step in general cases.

## 2.3 Reduced Order Modeling

A reduced order model (ROM) is a necessary tool for a fast and reasonably accurate prediction of the flow state; it is the basis of the feedback flow control strategy to reduce optical aberrations caused by distorted wave fronts. The distortions in wave fronts of an optical beam are directly related to density fluctuations due to the index-of-refraction, and the measure of the distortions can be expressed as the optical path length (OPL), as:

$$OPL = \int_0^l n(x,t)dx = \int_0^l K_{GD}\,\rho(x,t)dx \tag{11}$$

where $n(x,t)$ is the time and spatial variation of the index-of-refraction and $K_{GD}$ is the Gladstone-Dale constant, given as a function of the wavelength of the optical beam, $\lambda$ , [25] as:

$$K_{GD} = 2.23\times10^{-4}\left(1 + \frac{7.52\times10^{-15}}{\lambda^2}\right) \tag{12}$$

The wavelength used in this paper is $633nm$ , which corresponds to the wavelength of an He-Ne red laser.

The differences in OPL mean that the optical beam, which started with a collimated wave front, will have spatial and temporal variations and its focus and intensity will be reduced. These distortions of the wave front can be expressed as OPD by subtracting the average OPL over the aperture [10]:

$$OPD = OPL - \overline{OPL}^{x,z} \tag{13}$$

Assuming that the optical beam is propagated in the y-direction, an average in the x-z plane is subtracted. Since the OPD is a time dependent value, for simple comparison between the controlled results, RMS values of the OPD over time are considered.

Decomposing a set of data such as the OPD results of the open-loop controlled cases, according to the spatial and temporal characteristics and by the proper orthogonal decomposition (POD), is essential in building a low dimensional dynamic model. The spatial characteristics are decomposed in to spatial modes and temporal fluctuations are mapped onto each mode as the modal amplitudes, as [26,27]:

$$\varphi(x,t) = \sum_{j=1}^{J} a_j(t)\phi_j(x) \tag{14}$$

Since the time-varying OPD is a one-dimensional value, the resulting mode, $\phi_j(x)$, is also one-dimensional. The modal amplitudes, $a_j(t)$, are used in the ROM.

A class of neural network based ANN-ARX model is used as the ROM. An artificial neural network (ANN) is a biologically inspired mathematical model; the ANN-ARX is a simple model with signal "learning" capabilities. The input to output relationship is modeled as the sum of inputs, $x_i$, multiplied by their weights as a weighted sum [28]:

$$A_j(\bar{x},\bar{w}) = \sum_{i=0}^{n} x_i w_{ji} \tag{15}$$

and an activation function maps the weighted sum to the output. The most common activation function is the bipolar sigmoidal function:

$$O_j(\bar{x},\bar{w}) = \frac{2}{1+e^{O_j(\bar{x},\bar{w})}} - 1 \tag{16}$$

This bipolar sigmoid function returns a value of 1 for large positive numbers and -1 for large negative numbers. Such functions are used mainly because of their differentiability.

The weights are re-evaluated using the method of gradient descendent [29]:

$$\Delta w_{ji} = -\eta \frac{\partial E}{\partial w_{ji}} \tag{17}$$

where $E$ is the error sum of the given network:

$$E = \sum \left(O_j(\bar{x},\bar{w}) - d_j\right)^2 \tag{18}$$

This series of activation, error evaluation, and weight adjustment is carried out on each layer between the input and output (Figure 1).

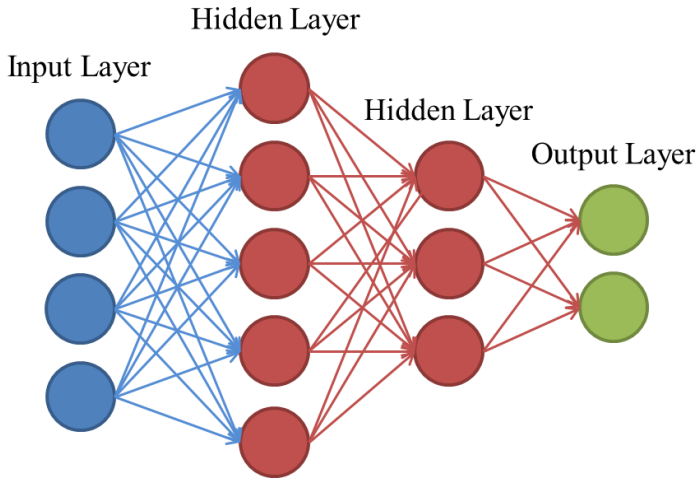


Figure 1: Example of artificial neural network.

# 3 Numerical Results

## 3.1 Validation

### 3.1.1 Flow characteristics and grid system

The physical properties of the Backward-Facing Step used by Driver and Seegmiller [18] are given in Table 1.

Table 1: Flow characteristics.

| | | |
|---|---|---|
| Step height | $h$ | $1.27cm$ |
| Reynolds number | $\mathrm{Re}_h$ | 38,000 |
| Freestream velocity | $U_\infty$ | $44.2m/s$ |
| Boundary layer thickness | $\delta$ | $1.9cm$ |
| Momentum thickness Reynolds number | $\mathrm{Re}_\theta$ | 5,000 |

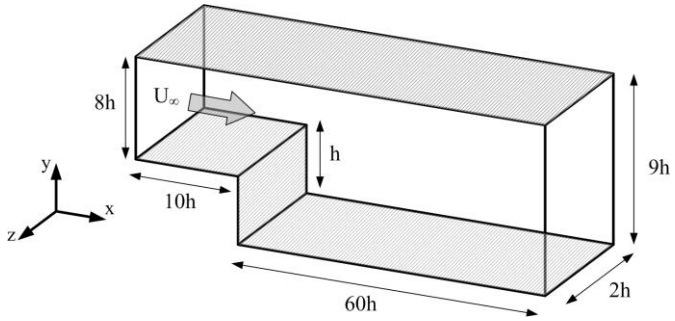

Figure 2: Schematic of BFS [18].

The step has an expansion ratio of 1.125, with the height of inlet as $8h$ and the exit as $9h$, where $h$ is the step height (Figure 2). The length of the inlet is 10h and the exit is placed at 60h downstream. The isothermal viscous wall boundary condition is applied to the top and bottom wall, and the periodic boundary condition is applied in the z-direction. The specified turbulent boundary layer and the constant pressure outflow boundary condition are applied to the inlet and outlet, respectively. For the inlet turbulent boundary layer profile, the velocity profile and kinematic eddy viscosity profile are generated from the EDDYBL program, written by Wilcox [30]. As can be seen from Figure 3, the generated profile follows the law of the wall very well.

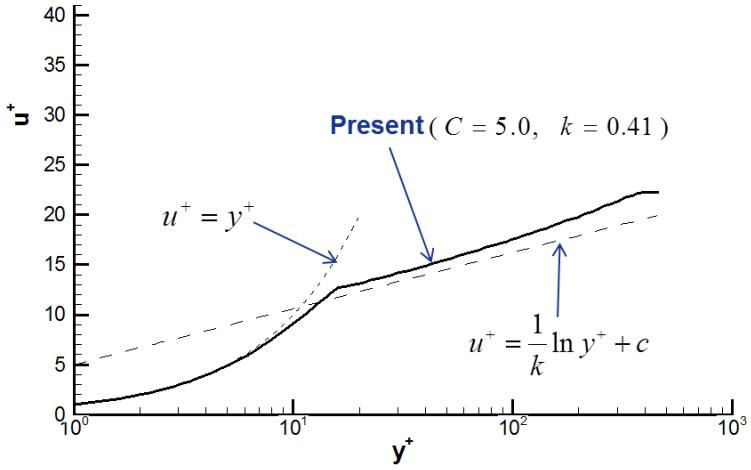

Figure 3: Specified turbulent boundary layer velocity profile in subgrid scale.

To test the implemented S-A DDES method on the length scale (Equations 8 and 9), three different grids have been tested for validation: a coarse grid (Grid-C) with 96,000 cells ($21\times21\times17$ for the inlet section before the step, $141\times41\times17$ for the section immediately after the step), a medium grid (Grid-M) with 268,800 cells ($21\times41\times17$ and $201\times81\times17$), and a fine grid (Grid-F) with 499,200 cells ($41\times61\times17$ and $241\times121\times17$). For all grids, the first cell distance from the wall in the subgrid scale is, $x^+, y^+ = 0.1$ and equally spaced in the z-direction. The time step used in the calculation is $\Delta t = 0.025h/U_\infty$ and 80 sub-iterations are used for the pseudo-time convergence at each physical time step.

### 3.1.2 Validation results

For comparison with the experiment, time-averaged S-A DDES results are used. Pressure coefficients and skin friction coefficients at the lower wall are compared with the experimental data in Figure 4 and Figure 5, respectively. In comparing the length scale, the maximum method, using Equation (8), shows large discrepancies with the experimental results. This is obvious in the sense that all grids have equal spacing in the z-direction and have $\Delta z$ as the maximum length. These results clearly show that the maximum method requires more grid points in the periodic direction. Meanwhile, the volume method, using Equation (9), shows good correlation with the experimental data when the medium (Grid-M) or fine grid (Grid-F) is applied.

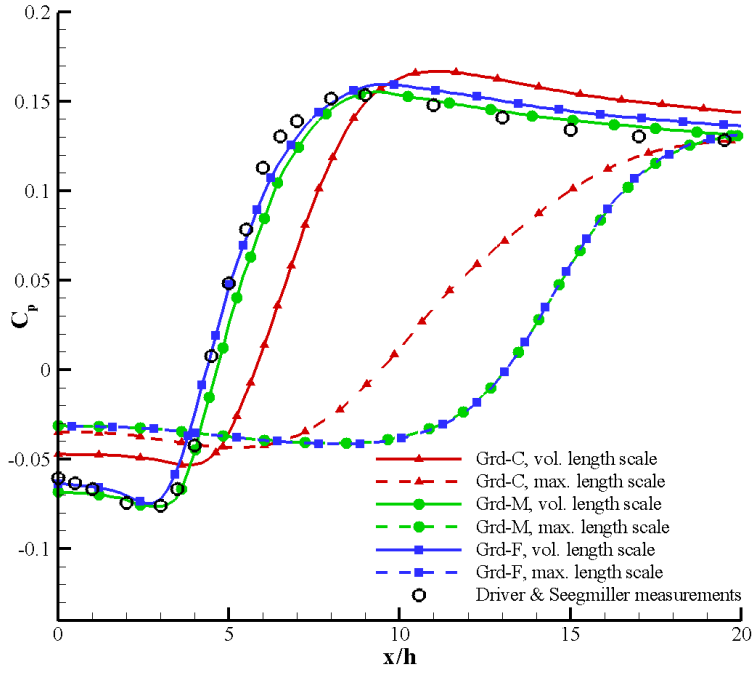


Figure 4: Pressure coefficient comparison.

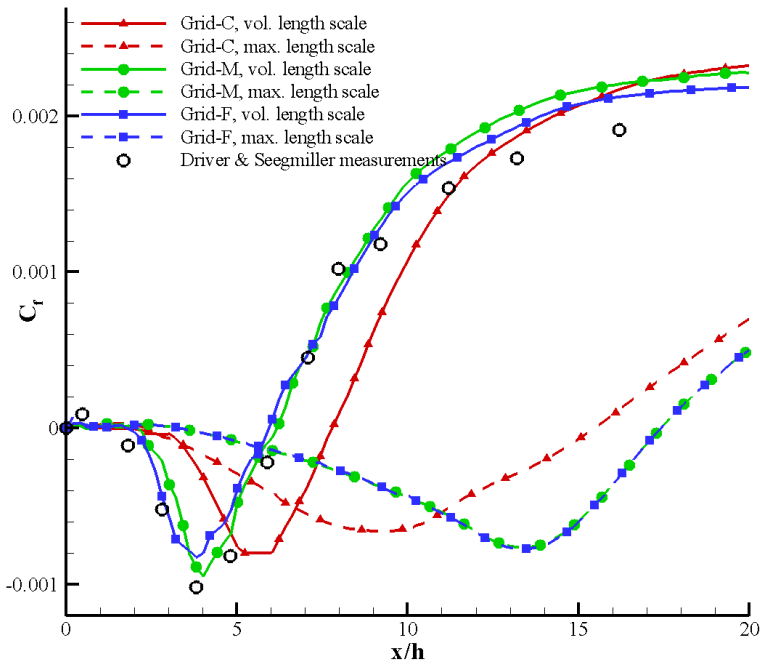


Figure 5: Skin friction coefficient comparison.

Table 2: Comparison of the reattachment length.

| | Grid-C | Grid-M | Grid-F |
|---|---|---|---|
| Max. length scale (Equation. 8) | 15.46 | 17.41 | 17.40 |
| Vol. length scale (Equation. 9) | 7.79 | 6.17 | 5.93 |
| Experiment [18] | | 6.20 | |

The computed reattachment length, shown in Table 2, also shows that using the cubic root of the cell volume reduces the effect of grid sizes in the periodic direction. Therefore, open-loop forced simulations adopt the volume method for the DDES length scale and the grid of medium density with 268,800 cells ( $21\times41\times17$ and $201\times81\times17$ ).

The medium-grid results are investigated further for the OPD and for the frequency analysis. The OPD is first calculated while assuming that a collimated light source is placed over a range from $x/h=0$ through to $x/h=10$. As shown in Figure 6 a) and b), the instantaneous OPD is very closely related to the vorticity, having large fluctuations in the proximity of vortical structures. The RMS of the OPD in Figure 6 c) shows that the fluctuation is greatest near $x/h=4$, where the fully developed vortical structures are breaking up. Therefore, the RMS of the OPD from $x/h=3.8$ to $x/h=4.2$ is chosen as the point at which the reduction of OPD will be assessed.

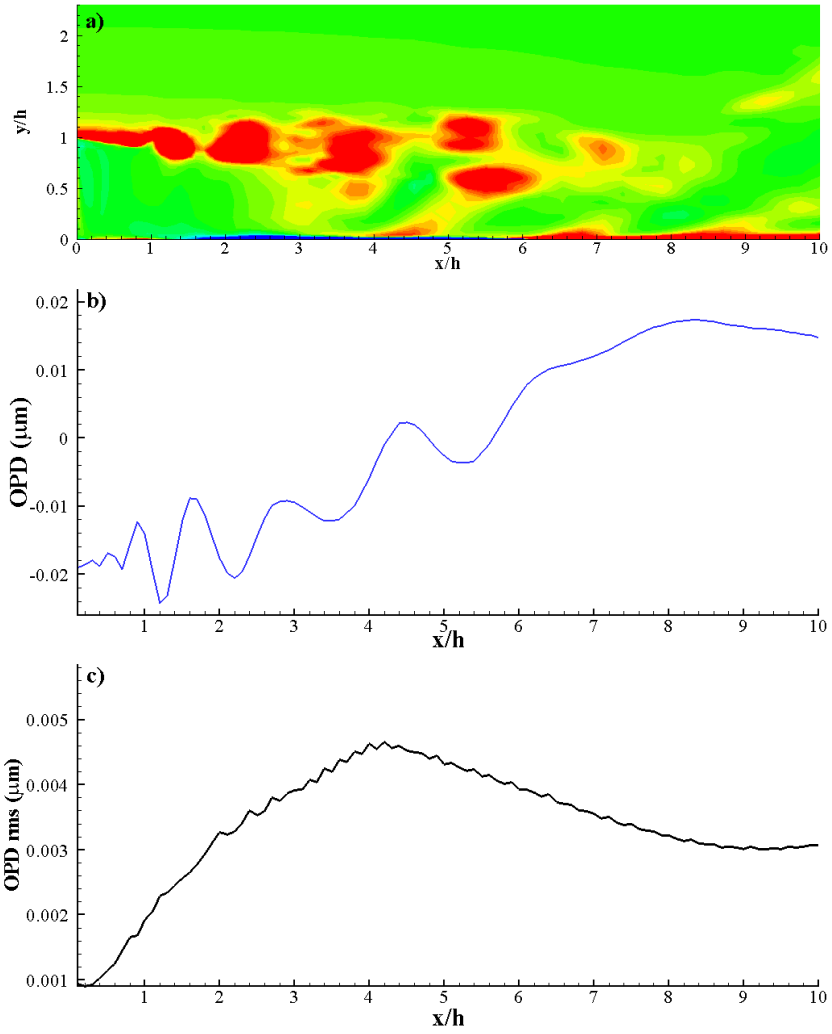


Figure 6: Instantaneous vorticity contour (a) and OPD (b) and RMS of OPD (c).

The frequency spectrum shown in Figure 7 is obtained from the streamwise velocity component at point $(x/h=6,\ y/h=1)$. From these results, the most dominant frequency was found to be $0.095f\,h/U_\infty$, which corresponds to the experimental value of $0.096f\,h/U_\infty$. The frequencies immediately next to the dominant frequency are $0.063f\,h/U_\infty$ and $0.125f\,h/U_\infty$. These frequencies, along with the dominant frequency, are used as the actuation frequencies for the open-loop forced simulations.

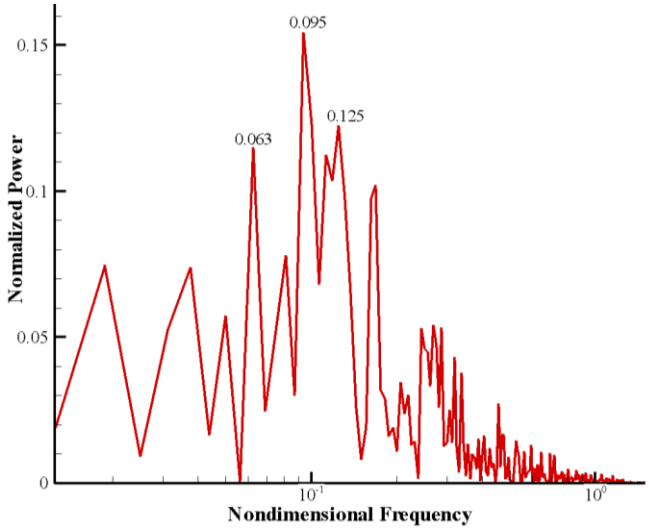


Figure 7: Frequency spectrum of streamwise velocity.

## 3.2 Open-loop Controlled Simulation Results

Open-loop controlled simulations are performed by numerically implementing a blowing and suction actuator at the edge of the step (Figure 8). The length of the actuator inlet is $1mm \approx 0.08h$ and the blowing and suction direction is tilted upwards by 45° to directly affect the shear layer being generated above the actuator. For the actuator boundary conditions, a parabolic velocity profile is assumed with blowing and suction velocity, $U_{BS}$, as:

$$U_{BS} = A_0\, Sin(2\pi wt) \tag{19}$$

where $A_0$ is the amplitude and $w$ is the frequency.

The actuation frequencies are decided from the previous validation case: $0.063f\,h/U_\infty$, $0.095f\,h/U_\infty$, and $0.125f\,h/U_\infty$ in real-time. The corresponding frequencies are $200Hz$, $330Hz$, and $400Hz$, respectively. For simplicity, $200Hz$, $300Hz$, and $400Hz$ are used as actuating frequencies. The actuating amplitudes used for the present computations are 1%, 2%, 3%, 4%, and 5% of the freestream velocity. 15 open-loop controlled cases in total are computed to establish the reduced order model.

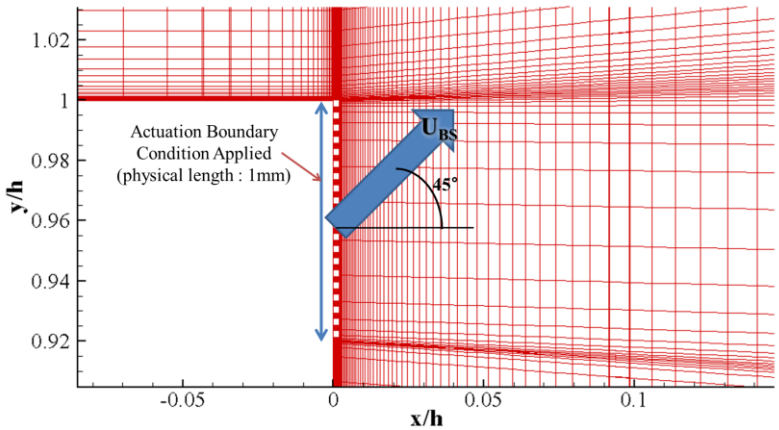


Figure 8: Implementation of blowing and suction boundary condition.

All simulation cases are carried out over a time period of 500 non-dimensional time period ($\approx 0.145s$ in real-time). To include the transient effect of the actuator, each computation starts with the actuator-off condition; the actuator is turned on after 100 non-dimensional seconds and turned off at 400 non-dimensional seconds.

The RMS of the OPD for all cases is displayed in Figure 9 at each actuation frequency. It can be seen clearly that the OPD fluctuation can be reduced with the given actuation velocity and frequency.

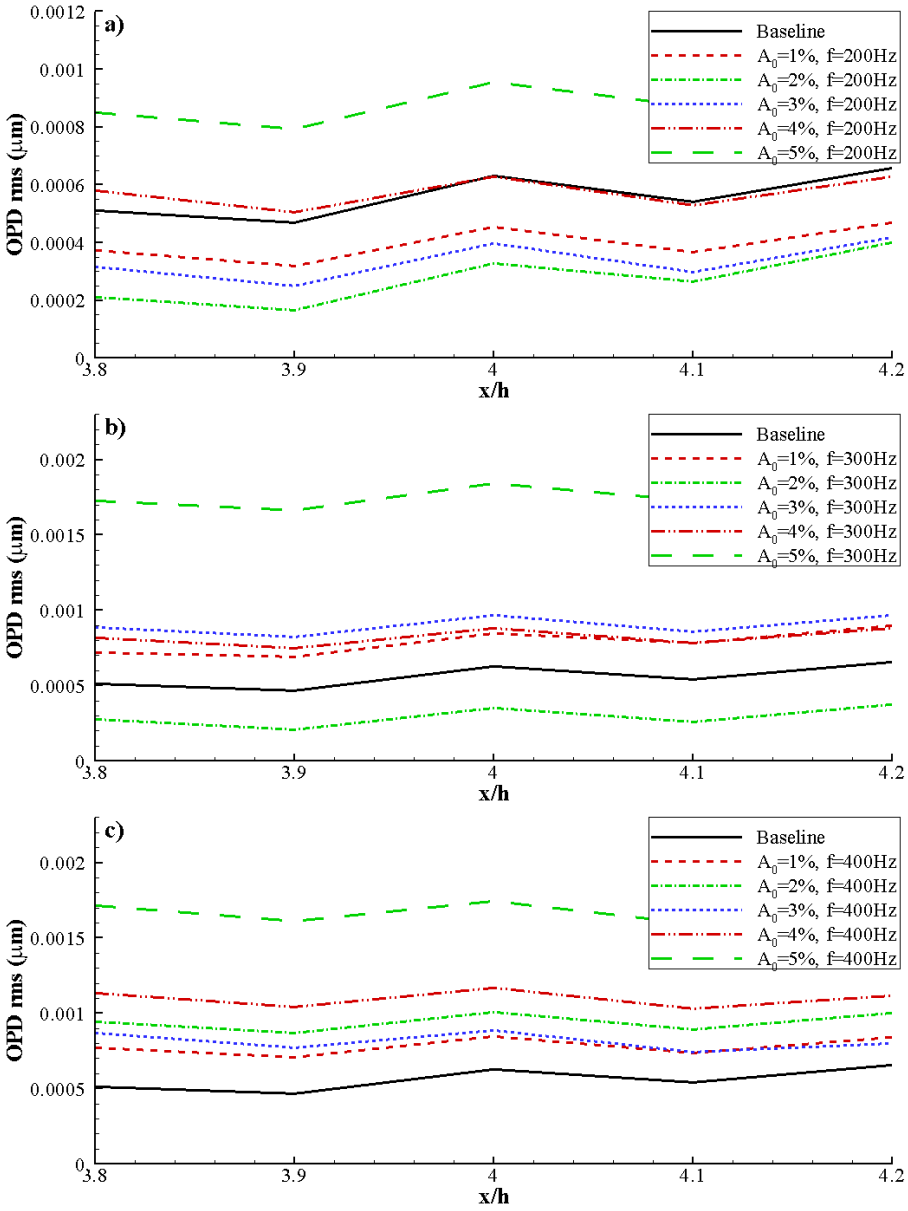


Figure 9: RMS of OPD comparison for all open-loop simulation cases.

To identify the mode that is responsible for the reduction of OPD RMS, the modal energy levels for the first four modes are compared in Figure 10. Figure 10 a) shows the modal energy for the $200Hz$ actuation cases; Figure 10 b) is for $300Hz$, and Figure 10 c) is for $400Hz$. The results show similar trends in all of the first four modes; however, having the largest energy, the first and the second modes are affected the most. Especially for the $200Hz$ actuation cases, the energy magnitudes of the first and the second modes for the 1%~3% results are attenuated compared to the baseline case. Reducing the modal amplitude of the first mode, therefore, is adopted as the feedback control strategy to reduce optical aberrations.

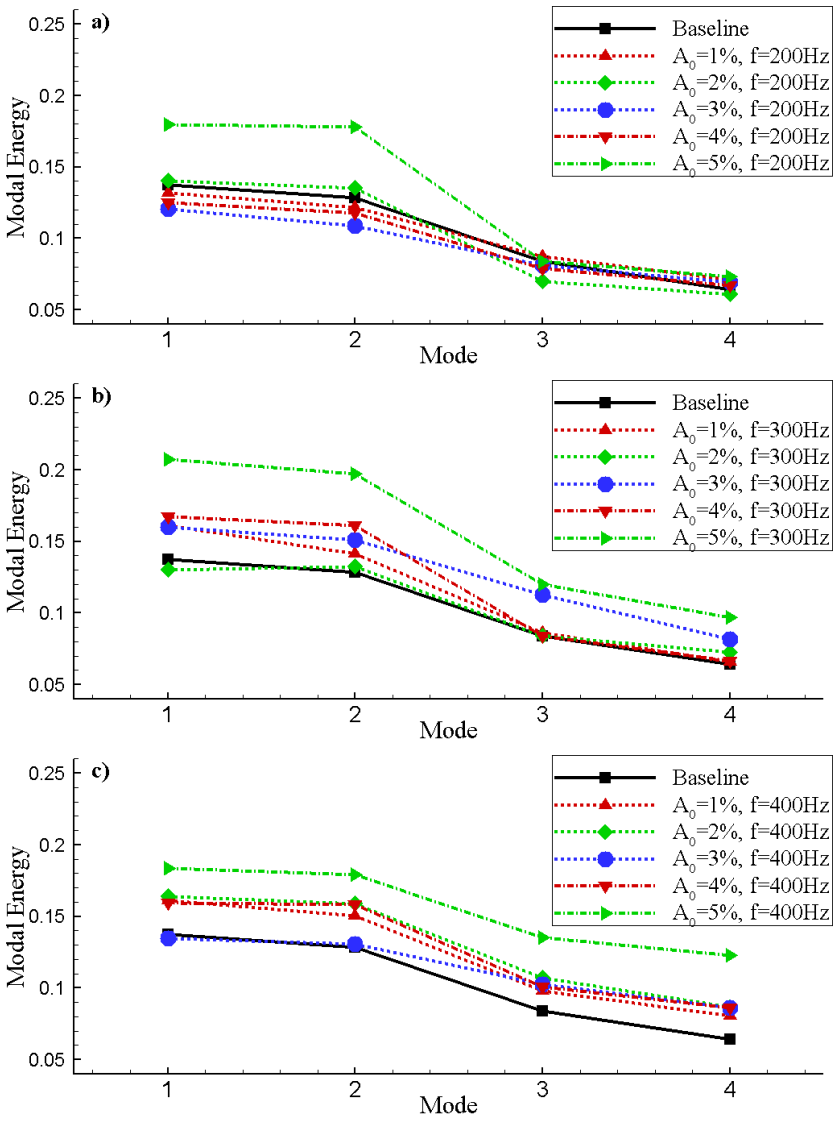


Figure 10: Modal energy comparison for all open-loop simulation cases.

## 3.3 ANN-ARX Predictor Validation

The accuracy of the ROM is validated first by training the ANN-ARX for a few cases and by using the ROM to predict off-design cases, which it has not been trained with. Table 3 summarizes the trained cases and off-design validation cases that are used.

Table 3: Trained and validation cases.
(○: Trained cases, ∆: Off-design validation cases)

| Actuation Amplitude | Actuation Frequency | | |
|---|---|---|---|
| | 200Hz | 300Hz | 400Hz |
| 1% | ○ | ○ | X |
| 2% | ∆ | ∆ | X |
| 3% | ○ | ○ | X |
| 4% | X | X | X |
| 5% | X | X | X |

An example of an on-design case and an off-design case are shown in Figure 11. The on-design case is the prediction of the actuation velocity and the frequency in which the ROM is trained. The off-design case, on the other hand, is simulated using the same off-on-off actuation, but with different actuation velocity and frequency. The present ROM reproduced the on-design case very well. Although it could not be expected for the prediction to duplicate the off-design case exactly, even the transient section ( $400 \le t$ ), as well as the unforced section ( $0 \le t \le 100$), is captured well.

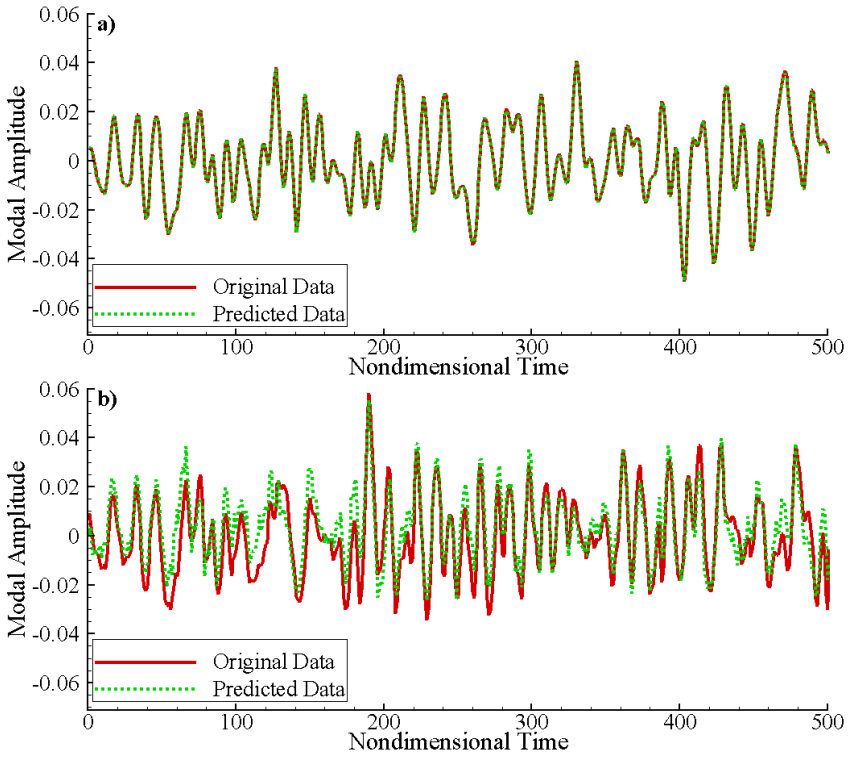


Figure 11: ROM validation for two cases;
a) on-design case: 1% amplitude and 200Hz actuation,
b) off-design case: 2% amplitude and 300Hz actuation.

## 3.4 Feedback Controlled Results

The feedback controller designed with the objective of reducing the optical aberrations is schematically illustrated in Figure 12. The ANN-ARX model is used to predict the modal amplitudes for given the actuation velocity; the feedback controller uses the predicted modal amplitude to obtain the new actuation velocity using Equation 20.

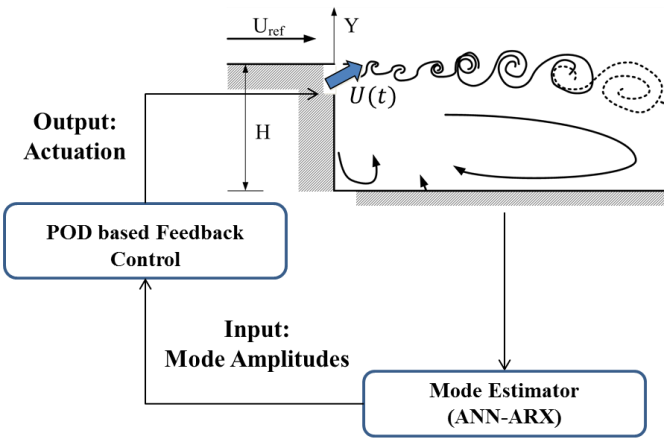


Figure 12: Feedback Control Flowchart.

$$U_{BS} = K_p a_1 + K_d \frac{da_1}{dt} \tag{20}$$

where $a_1$ is the modal amplitude of the first mode and $K_p, K_d$ are the proportional gain and derivative gain, respectively. In order to minimize the modal amplitudes, the gains obtained are $K_p = -0.2,\ K_d = 0.1$.

The modal amplitude prediction and the actuation velocity of the feedback controller are shown in Figure 13. The actuation velocity is shown to be smaller than those of the simulated cases (smaller than 1%); however, velocities smaller than 1% are accounted for in the time varying input velocity.

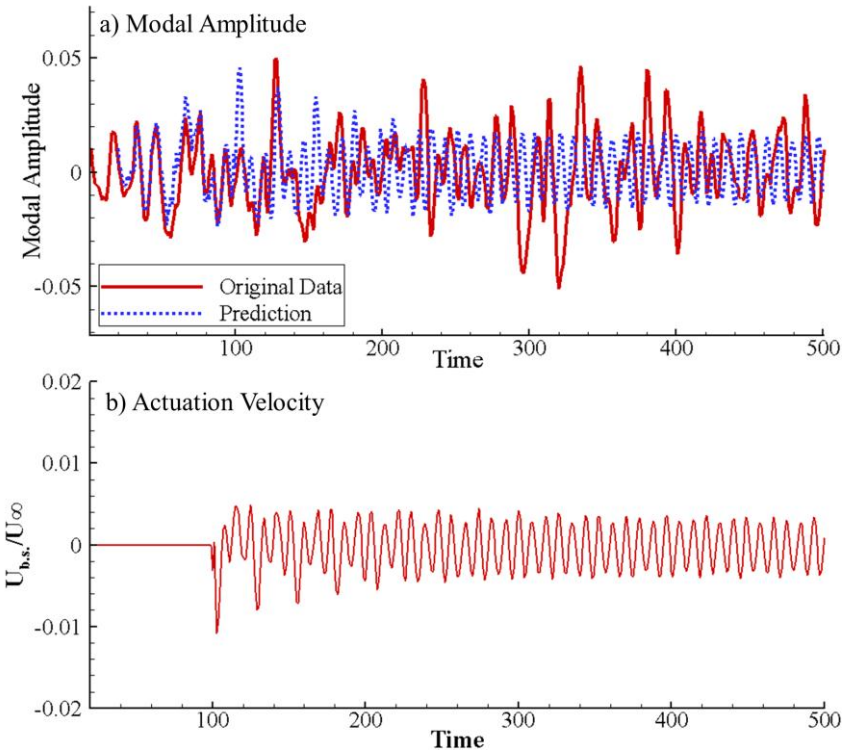


Figure 13: ROM prediction of modal amplitude and actuation velocity.

The feedback controller is validated with three-dimensional S-A DDES simulation using the actuation velocity obtained from the controller (Figure 13 b). The result from the simulation is averaged in the z-direction to calculate the OPD; the OPD results are then decomposed using the POD method to obtain modal amplitudes. The modal amplitudes of the simulation using the feedback-controlled actuation velocity are shown in Figure 14; the RMS of OPD is shown in Figure 15.

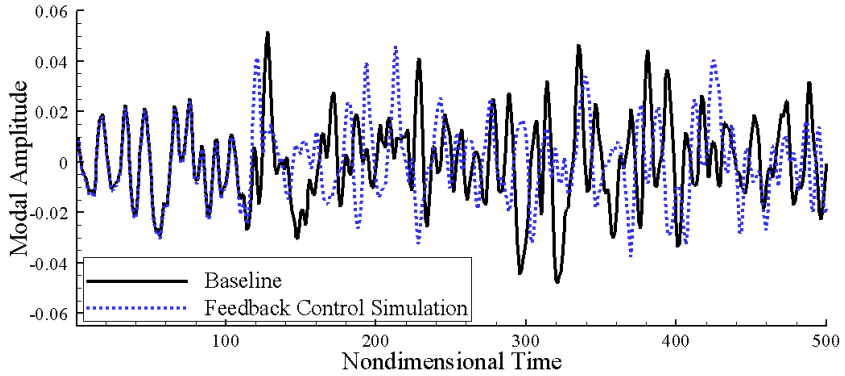


Figure 14: Modal amplitude comparison with feedback control results and baseline case.

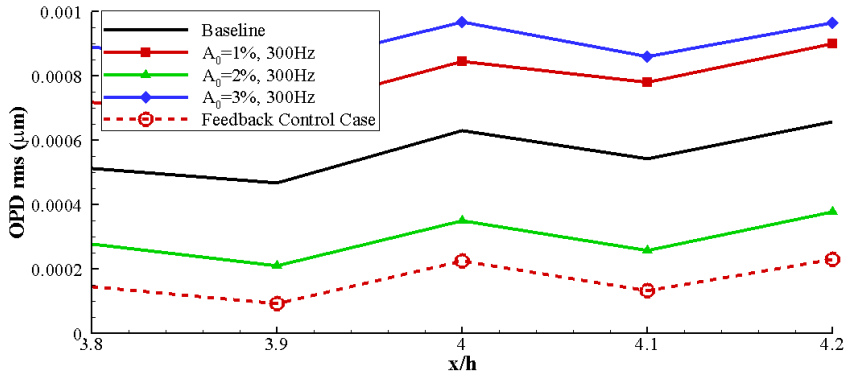


Figure 15: RMS of OPD comparison with the feedback control results.

The numerical results using the feedback-controlled actuation velocity indicate that the modal energy of the first mode was reduced by 17% and that of the second mode was reduced by 19% from the baseline case. Furthermore, Figure 15 shows that a large reduction, up to 60%, in the OPD RMS has been achieved with the present feedback control.

# 4 Concluding Remarks

A three-dimensional S-A DDES simulation has been successfully used in the designing of a feedback flow controller for turbulent flows over a backward facing step. The numerical results for the unforced baseline case showed good agreement with the experimental data of Driver and Seegmiller [18]. The pressure coefficients and the skin-friction coefficients were well predicted using the cubic root of the cell volume as the DDES length scale. The dominant frequencies of the streamwise velocity near the reattachment position were used as the actuating frequencies for the open-loop forced simulations. The POD results of the open-loop forced simulations showed that reducing the first mode's modal amplitude can mitigate optical aberrations near the $x/h = 4$ region. The ANN-ARX model predicted the off-design cases with good accuracy. A simple control strategy to reduce the modal amplitude of the first mode resulted in a decrease in the OPD RMS of 60%, compared to the unforced baseline simulation.

# Acknowledgement

The authors gratefully acknowledge the financial support provided by the Agency for Defense Development of Korea (UD100055CD).

# References

[1] K. G. Gilbert and L. J. Otten. Aero-Optical Phenomena. Progress in Astronautics and Aeronautics, Vol. 80, pp. 1-9, AIAA, New York, 1982.

[2] E. J. Jumper and E. J. Fitzgerald. Recent advances in aero-optics. Prog. Aero. Sci., Vol. 37, pp. 299-339, 2001.

[3] S. Gordeyev, T. E. Hayden and E. Jumper. Aero-Optical and Flow Measurements over a Flat-Windowed Turret. AIAA Journal, Vol. 45, No. 2, pp. 347-357, 2007.

[4] J. Cress, S. Gordeyev, M. Post and E. J. Jumper. Aero-Optical Measurements in a Turbulent, Subsonic Boundary Layer at Different Elevation Angles. 39th AIAA Plasmadynamics and Lasers Conference, 23-26 June, Seattle, 2008.

[5] J. Cress, S. Gordeyev and E. J. Jumper. Aero-Optical Measurements in a Heated, Subsonic, Turbulent Boundary Layer. 48th AIAA Aerospace Sciences Meeting, 4-7 Jan, Orlando, 2010.

[6] R. M. Rennie, J. P. Siegenthaler and E. J. Jumper. Forcing of a Two-Dimensional, Weakly-Compressible Subsonic Free Shear Layer. AIAA Paper 2006-0561, 2006.

[7] J. Cress, S. Gordeyev, E. Jumper, T. T. Ng and A. B. Cain. Similarities and Differences in Aero-

Optical Structure over Cylindrical and Hemispherical Turrets with a Flat Window. AIAA Paper 2007-0326, 2007.
[8] A. E. Smith, S. Gordeyev and E. Jumper. Aero Optics of Subsonic Boundary Layers over Backward Steps. 42nd AIAA Plasmadynamics and Lasers Conference, 27 June, Honolulu, 2011.
[9] D. J. I. Wittich, D. A. Duffin, E. J. Jumper, A. B. Cain and E. J. Kerschen. Passive Shear Layer Regularization Experiments in Wind Tunnels and Feed-Forward Adaptive-Optic Correction. AIAA Paper 2009-0358, 2009.
[10] J. Seidel, S. Siegel, T. McLaughlin and C. Fagley. Feedback Flow Control of a Shear Layer for Aero-Optic Applications. 48th AIAA Aerospace Sciences Meeting Including the New Horizons Forum and Aerospace Exposition, 4-7 January, Orlando, Florida, 2010.
[11] J. Seidel, S. Siegel, T. McLaughlin and C. Fagley. Reduced order modeling for feedback flow control of a shear layer. 5th Flow Control Conference, 28 June, Chicago, 2010.
[12] P. R. Spalart. W.-H. Jou, M. Streletsand S. R. Allmaras. Comments on the Feasibility of LES for Wings and on a Hybrid RANS/LES approach. Proceedings of first AFOSR international conference on DNS/LES, Louisiana, Greyden Press, 1997.
[13] P. R. Spalart and S. R. Allmaras. A One-Equation Turbulence Model for Aerodynamic Flows. AIAA paper 94-0643, 1992.
[14] P. Spalart, S. Deck, M. Shur, K. D. Squires, M. Strelets and A. Travin, A New Version of Detached-Eddy Simulation, Resistant to ambiguous Grid Densities, Theoretical Computational Fluid Dynamics, Vol. 20, pp. 181-195, 2006.
[15] A. Travin, M. Shur, M. Strelets and P. Spalart, Detached-Eddy Simulations Past a Circular Cylinder, Flow, Turbulence and Combustion Vol. 63, pp. 293-313, 1999.
[16] B. Sainte-Rose, N. Bertier, S. Deck, F. Dupoirieux, A DES method applied to a Backward Facing Step reactive flow, Comptes Rendus. Mecanique, Vol. 337, no. 6/7, pp. 340-351, 2009.
[17] J. Riou, E. Garnier, S. Deck and C. Basdevant, Improvement of Delayed-Detached Eddy Simulation Applied to Separated Flow Over Missile Fin. AIAA Journal, Vol. 47, No. 2, Feb. pp. 345-360, 2009.
[18] S. M. Driver and H. L. Seegmiller. Features of a Reattaching Turbulent Shear Layer in Divergent Channel Flow. AIAA Journal, Vol. 23, No. 2, pp. 163-171, 1985.
[19] S. Siegel, J. Seidel, C. Fagley, D. M. Luchtenburg, K. Cohen and T. McLaughlin. Low-dimensional modeling of a transient cylinder wake using double proper orthogonal decomposition. Journal of Fluid Mechanics, Vol. 610, pp. 1-42, 2008.
[20] J. M. Weiss and W. A. Smith, Preconditioning Applied to Variable and Constant Density Flows, AIAA Journal, Vol. 33, No. 11, pp. 2050-2057, 1995.
[21] S. H. Park, J. E. Lee and J. H. Kwon. A Preconditioned HLLE Method for Flows at All Mach Numbers. AIAA Journal, Vol. 44, No. 11, pp. 2645-2653, 2006.
[22] S. H. Park and J. H. Kwon. Implementation of k-w Turbulence Models in an Implicit Multigrid Method. AIAA Journal, Vol. 42, No. 7, pp. 1348-1357, 2004.
[23] G. Xia, S. Sardeshmukh, V. Sankaran and C. L. Merkle. Implementation of an Enhanced Flux Formulation for Unsteady Navier-Stokes Solutions. Proceedings of the Fourth International Conference on Computational Fluid Dynamics, ICCFD4, Ghent, Belgium, 10-14 July, 2006.
[24] S. A. Pandya, S. Venkateswaran and T. H. Pulliam. Implementation of Preconditioned Dual-Time Procedures in OVERFLOW. AIAA paper 2003-0072, 2003.
[25] D. T. Kyrazis. Optical degradation by turbulent free-shear layers. Proc. SPIE: Optical Diagnostics in Fluid and Thermal flow. Vol. 2005, pp. 170~181, 1993.
[26] L. Sirovich. Turbulence and the dynamics of coherent structures Part I: Coherent Structures, Applied Mathematics, Vol.45, No.3, pp. 561-571, 1987.
[27] R. Holmes, J. Lumley and C. Buckwalter. Turbulence, Coherent Structures, Dynamical Systems and Symmetry. Cambridge University Press. 1999.
[28] C. Lee, J. Kim, D. Babcockand R. Goodman. Application of neural networks to turbulence control for drag reduction, Physics and Fluids. Vol. 9, No. 6, pp. 1740-1747, 1997.
[29] M. Norgaard, O. Ravn, N. K. Poulsenand L. K. Hansen. Neural Networks for Modeling and Control of Dynamic systems. International Journal of Robust and Nonlinear Control, Vol. 11, No. 9, pp. 881-882, 2000.
[30] D. C. Wilcox. Turbulence Modeling for CFD. 2nd Edition, DCW Industries Inc. 2000.